On the nonlinear evolution of wind-driven gravity waves

A. Alexakis
Department of Physics, The University of Chicago, Chicago, Illinois 60637
and Center for Astrophysical Thermonuclear Flashes, The University of Chicago, Chicago, Illinois 60637

A. C. Calder and L. J. Dursi
Center for Astrophysical Thermonuclear Flashes, The University of Chicago, Chicago, Illinois 60637
and Department of Astronomy & Astrophysics, The University of Chicago, Chicago, Illinois 60637

R. Rosner
Department of Physics, The University of Chicago, Chicago, Illinois 60637;
Center for Astrophysical Thermonuclear Flashes, The University of Chicago, Chicago, Illinois 60637;
Department of Astronomy & Astrophysics, The University of Chicago, Chicago, Illinois 60637;
and Enrico Fermi Institute, The University of Chicago, Chicago, Illinois 60637

J. W. Truran
Center for Astrophysical Thermonuclear Flashes, The University of Chicago, Chicago, Illinois 60637;
Department of Astronomy & Astrophysics, The University of Chicago, Chicago, Illinois 60637;
and Enrico Fermi Institute, The University of Chicago, Chicago, Illinois 60637

B. Fryxell
Center for Astrophysical Thermonuclear Flashes, The University of Chicago, Chicago, Illinois 60637
and Enrico Fermi Institute, The University of Chicago, Chicago, Illinois 60637

M. Zingale
Department of Astronomy and Astrophysics, The University of California, Santa Cruz, Santa Cruz, California 95064

F. X. Timmes
Center for Astrophysical Thermonuclear Flashes, The University of Chicago, Chicago, Illinois 60637
and Department of Astronomy & Astrophysics, The University of Chicago, Chicago, Illinois 60637

K. Olson
Department of Physics, The University of Chicago, Chicago, Illinois 60637
and UMBC/GEST Center, NASA/GSFC, Greenbelt, Maryland 20771

P. Ricker
Center for Astrophysical Thermonuclear Flashes, The University of Chicago, Chicago, Illinois 60637

We present a study of wind-driven nonlinear interfacial gravity waves using numerical simulations in two dimensions. We consider a case relevant to mixing phenomenon in astrophysical events such as novae in which the density ratio is approximately 1:10. Our physical setup follows the proposed mechanism of Miles [J. Fluid Mech. **3**, 185 (1957)] for the amplification of such waves. Our results show good agreement with linear predictions for the growth of the waves. We explore how the wind strength affects the wave dynamics and the resulting mixing in the nonlinear stage. We identify two regimes of mixing, namely, the overturning and the cusp-breaking regimes. The former occurs when the wind is strong enough to overcome the gravitational potential barrier and overturn the wave. This result is in agreement with the common notion of turbulent mixing in which density gradients are increased to diffusion scales by the stretching of a series of vortices. In the latter case, mixing is the result of cusp instabilities. Although the wind is not strong enough to overturn the wave in this case, it can drive the wave up to a maximum amplitude where a singular structure at the cusp of the wave forms. Such structures are subject to various instabilities near the cusp that result in breaking the cusp. Mixing then results from these secondary instabilities and the spray-like structures that appear as a consequence of the breaking. © *2004 American Institute of Physics.*
[DOI: 10.1063/1.1771695]

I. INTRODUCTION

The generation of surface waves by winds has been studied for well over a century. Helmholtz[1] and Lord Kelvin[2] investigated the stability of fluid interfaces using a simple step function wind shear profile (see Ref. 3 and references therein for further discussion). The formulation has been extended to weakly nonlinear[4] and fully nonlinear regimes[5] (see also Ref. 6 for more recent developments). It was noticed early on that the Kelvin–Helmholtz theory (from now on KH) predicted that instability occurred only for wind velocities greater than a minimum velocity; this limit was in-
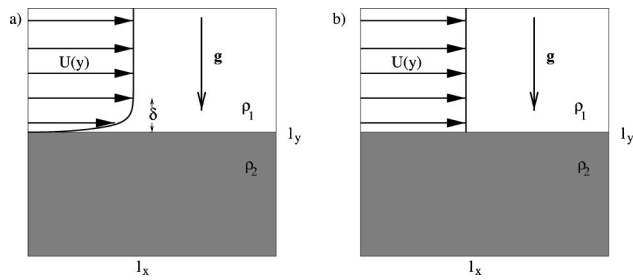
FIG. 1. Panel (a) shows a sketch of the wind profile used in out simulations. Panel (b) shows the wind profile assumed by the simplest Kelvin–Helmholtz instability studies.

consistent with observations on the ocean.[7] This puzzle was resolved with the work of Miles,[8] which showed that waves can be amplified by a resonant mechanism. Instead of working with a step function velocity profile, Miles assumed that the upper (lighter) fluid was moving with velocity given by $U(y) = U^* f(y/y^*)$, where y is the distance from the interface and U^* and y^* are a characteristic velocity and length scale, respectively, of the wind [see Fig. 1(a)]. f is a function that Miles estimated from boundary layer theory. Detailed calculations from linear theory then show that there is an influx of energy from the wind to the gravity wave as long as there is a height at which the wind velocity equals the phase velocity of the gravity wave.[8,9] At this height, the linear eigenvalue problem is singular and a "critical layer" is formed. The formation of this critical layer allows the pressure perturbation to be in phase with the slope of the wave rather than its trough, thus driving the wave unstable. Vortices that travel with the same velocity as the wave (i.e., a resonant condition) therefore amplify it. The resulting minimum velocity to excite gravity waves is smaller by a factor of $\sqrt{\rho_1/\rho_2}$ than the minimum velocity obtained by KH theory and is in much better agreement with experiments and observations.

Our interest in this problem comes from a similar astrophysical puzzle—the upward mixing of heavier core elements (carbon and oxygen, henceforth C/O) into a lighter (hydrogen–helium) atmosphere in precursors to classical nova explosions. The nova outburst results from the ignition and subsequent explosive thermonuclear burning of a hydrogen-rich layer that has accreted onto the surface of a C/O white dwarf from a stellar companion.[10–12] Abundances and explosion energies measured from observations indicate that there must be significant mixing of the heavier material (C/O) of the white dwarf into the lighter accreted material (H/He). Accordingly, nova models must incorporate a mechanism that will dredge up the heavier white dwarf material. The exact mechanism of the dredge up process that leads to the required enrichment has been the subject of considerable research over the last two decades. The dredge up mechanism will determine the frequency and energetics of nova outbursts,[13–15] and so it must be included in any detailed model of novae.

Rosner et al.[16] proposed that breaking gravity waves can give the required mixing in a similar manner to that of water mixing into the atmosphere above an ocean (see also Ref. 17 for recent results). In the case of the novae, wind originating

either from the accretion process itself or by thermally driven convection can amplify and break gravity waves on the surface of the white dwarf, thereby enriching the accreted material with material from the surface. In this astrophysical case, although the two fluid layers involved (accreted H/He envelope and white dwarf C/O) are miscible, diffusion length scales are so small that the waves formed (prior to mixing by large scale motions) can be considered as interfacial.

In applying this breaking gravity wave mechanism to the stellar case, one must generalize the earlier results to arbitrary density ratios. This study has been done for the linear problem,[18] deriving bounds on instability in parameter space and estimating growth rates of unstable modes. For the weakly nonlinear problem, the asymptotic case of a weak wind has been studied in Ref. 19. However, linear and weakly nonlinear theories give little direct information about mixing, which is largely governed by nonlinear processes.

For the generation of gravity waves in the oceans there is a vast literature on modeling wave growth and breaking. Description of some of the most recent models and aspects of present investigations can be found in Refs. 20 and 21 and references therein. The derived models are based both on theoretical arguments and a large pool of observational data. However, to our knowledge, the fully nonlinear evolution of the resonant instability has not been previously studied with direct numerical simulations for either the case of the ocean or the astrophysical problem. The oceanographic problem is difficult to address numerically both because the difference in densities between the two fluids ($\rho_{air}/\rho_{water} = 10^{-3}$) makes the growth time scale one thousand times smaller than the wave period and because surface tension plays a key role in the spray formation. Nonetheless, there have been numerical investigations of boundary layer simulations in the presence of wavy boundaries[22,23] and the effect of "waves" on the wind profile was studied. Present computational resources make more detailed modeling of the oceanographic problem with numerical simulations difficult. However, it is possible to address the astrophysical problem for a range of relatively strong winds.

In this paper we present results of the fully nonlinear problem of wind driven gravity waves for fixed density ratio of $\rho_1/\rho_2 = 0.1$. The simulations in this study were performed using the FLASH code,[24–26] a parallel, adaptive-mesh hydrodynamics code for the compressible flows found in astrophysical environments.

The paper is structured as follows. In Sec. II we present the physical setup used in our simulation studies and the equations of motion. In Sec. III we present a short summary of the linear and weakly nonlinear theories as well as the theory of free traveling waves. In Sec. IV we discuss the numerical code used for the simulations, and in Sec. V we present the table of our runs and justify the choice of the parameter space we examine. Section VI presents results about the wave dynamics we observe. In Sec. VII we present and discuss our results about mixing and in Sec. VIII we present our convergence studies. We summarize and draw our conclusions in Sec. IX.

II. INITIAL SETUP AND EVOLUTION EQUATIONS

We consider a two-dimensional square box of size $l_y = l_x$, with two layers of compressible fluid in hydrostatic equilibrium separated by a sharp interface located at $l_y/2$. The densities of the fluids are ρ_1 immediately above the interface and ρ_2 immediately below, with $\rho_1 < \rho_2$. There is a uniform gravitational field $\mathbf{g}$ in the negative y direction. The upper fluid moves in the x direction with a velocity given by $U(y)$, where $y = 0$ corresponds to the location of the unperturbed interface. The exact form of $U(y)$ used is

$$U(y) = U_{\max}(1 - e^{-y/\delta}), \tag{1}$$

where δ is a characteristic length scale. A sketch of the wind profile is shown in Fig. 1 (a) where it is compared with profile used by KH (b).

The equations we evolve are the compressible Euler equations for inviscid flow,

$$\frac{\partial \rho}{\partial t} + \mathbf{\nabla} \cdot \rho\mathbf{v} = 0, \tag{2}$$

$$\frac{\partial \rho\mathbf{v}}{\partial t} + \mathbf{\nabla} \cdot \rho\mathbf{v}\mathbf{v} + \mathbf{\nabla} P = \rho\mathbf{g}, \tag{3}$$

$$\frac{\partial \rho E}{\partial t} + \mathbf{\nabla} \cdot (\rho E + P)\mathbf{v} = \rho\mathbf{v} \cdot \mathbf{g}, \tag{4}$$

where ρ is the density, $\mathbf{v}$ is the fluid velocity, P is the pressure, and $\mathbf{g}$ is the acceleration due to gravity. E is the total specific energy, composed of the specific internal energy ϵ and the kinetic energy per unit mass,

$$E = \epsilon + \tfrac{1}{2}v^2. \tag{5}$$

The system of equations must be closed by an equation of state of the form $P = P(\rho, \epsilon)$, for which we use a simple γ law,

$$P = (\gamma - 1)\rho\epsilon. \tag{6}$$

The initial density and pressure profiles were obtained by integrating the equation of hydrostatic equilibrium in an isotropic atmosphere,

$$\frac{dP}{dy} = -\rho g\hat{y}, \tag{7}$$

which for the case of a compressible γ-law gas gives

$$\rho|_{t=0} = \rho_i \left[1 - (\gamma - 1)\frac{g\rho_i y}{P_0 \gamma} \right]^{1/(\gamma-1)} \quad \text{and} \quad P = P_0 \left(\frac{\rho}{\rho_i} \right)^{\gamma}. \tag{8}$$

Here P_0 is the pressure at the interface and $\rho_{i=1,2}$ is the density immediately above or below the interface.

A passive scalar X representing the mass fraction of a species is advected by

$$\frac{\partial \rho X}{\partial t} + \mathbf{\nabla} \cdot \rho X\mathbf{v} = 0. \tag{9}$$

The mass fraction $X_i(t, \mathbf{x})$ of a species i represents the ratio of the mass m_i of the species i included in an infinitesimal

volume element located at $\mathbf{x}$ at time t, to the total mass m included in the same volume element. In our approach we introduce the passive scalar X representing the mass fraction of the lower fluid so that X takes initially the value 1 below the interface and 0 above.

We use periodic boundary conditions in the x direction and hydrostatic, stress-free boundary conditions in the y direction.[27] We note that we perform "run down" simulations in the sense that after the initial conditions are set, no additional forcing is used to maintain the wind flow.

The nondimensional numbers involved are $G = g\delta/U_{\max}^2$, which gives a measure of the strength of the wind (G is related to the Froude number F as $G = F^{-2}$), the density ratio $r = \rho_1/\rho_2$ immediately above and below the interface [or equivalently the Atwood number $A_t = (1-r)/(1+r)$], and the Mach number given by $M = U_{\max}/C_s$, where C_s is the sound speed in the upper fluid given by $C_s = \sqrt{\gamma(P/\rho_1)}$. Two additional numbers appear due to the finite size of our calculation. The first one is $L = l_x g/U^2$, which is a measure of the size of the box we are using. The second one is N, which gives the size of our grid for each spatial direction. Because there is no explicit viscosity, the effective Reynolds number of the flow is an increasing function of N, although an exact relation between the two is hard to obtain.

We use simple sinusoidal perturbations of small amplitude to initialize the gravity waves. For single-mode calculations the perturbed interface was written as

$$h(x) = A \cos(k_0 x), \tag{10}$$

where $k_0 = 2\pi/l_x$ is the smallest wave number that fits the computational domain and A is the amplitude of the wave. In the lower fluid the perturbation of the velocity was decreasing exponentially according to the results of the linear theory. In the upper fluid the velocity perturbations were modeled so as to mimic the eigenfunctions of the linear problem. Ak_0 was set to 0.05. For multimode perturbations, a superposition of different modes was used with random phases. The exact form of the interface is

$$h(x) = \sum A_k \cos(kx + \phi_r), \tag{11}$$

where ϕ_r is a random function and the amplitude A_k of each excited mode is given by $A_k = C_{k_{\max}} k e^{-k/k_{\max}}$. $C_{k_{\max}}$ is a normalizing coefficient keeping the total amplitude of the perturbation equal to 0.05. $k_{\max}$ was set to $2k_0$ for all runs except those in which the effect of the initial spectrum was studied. For all simulations, we kept r fixed at 0.1 and tried to minimize the effects of compressibility by keeping $M = 0.2$. Our principal aim, therefore, is to investigate how gravity wave generation and mixing is affected as we change the parameter G in the limits $L \to \infty$ and $N \to \infty$.

III. GRAVITY WAVES, LINEAR AND WEAKLY NONLINEAR THEORIES

Linear theory is always to be examined first in the study of an instability. Although it is not informative about the fully nonlinear structures the system develops, it imposes constraints on the spectrum of the unstable modes and determines the time scales involved given by the linear growth

rate. Furthermore, weakly nonlinear theories help in understanding asymptotic regimes of the instability. Finally, there are many known results about finite amplitude free waves (no driving) that are found to be relevant in our research. In the subsections below we give a brief review of the results of linear and weakly nonlinear theories and the theory of finite amplitude free waves.

A. Linear theory

Starting with the background described in Sec. II, introducing small sinusoidal perturbations and keeping only the linear terms of the perturbation in Eqs. (2) and (3) leads to the following eigenvalue problem:

$$\phi'' - \left(k^2 + \frac{U''}{U-c}\right)\phi = 0 \qquad (12)$$

with

$$\rho_2 kc^2 - \rho_1[c^2\phi'|_0 + cU'|_0] - g(\rho_2 - \rho_1) = 0 \qquad (13)$$

at $y=0$. Here k is the wave number of the perturbation, c is the phase velocity of the wave, and the stream function of the flow is given by $\Psi = \phi(y)e^{ikx} + \phi^*(y)e^{-ikx}$. Incompressibility has been assumed to simplify the analysis. The imaginary part of c times k gives the growth rate. One can prove the following from the above equations. All unstable waves have phase velocity smaller than $\max(U)$, i.e., the wind cannot excite waves traveling faster than its maximum velocity. Furthermore, Howard's semicircle theorem holds: $(\mathrm{Re}\{c\})^2 + \mathrm{Im}\{c\}^2 \leqslant \max\{U\})$. For a wind profile given by $U(y) = U_{\max}(1 - e^{y/\delta})$ the smallest unstable wave number to the resonant instability is given by[18]

$$k_R = \left(\frac{1}{\delta}\right)\frac{G(1-r) + r - r\sqrt{[G(1-r)+r]^2 + (1-r^2)}}{1-r^2}. \qquad (14)$$

In the limit of small G investigated in this paper, we have that

$$\frac{2\pi}{\lambda_R} \equiv k_R \simeq \frac{g}{U_{\max}^2}(1 - \rho_1/\rho_2). \qquad (15)$$

The above result should be compared with that predicted by KH theory given by

$$\frac{2\pi}{\lambda_{KH}} \equiv k_{KH} = \frac{\rho_2^2 - \rho_1^2}{\rho_1\rho_2}\frac{g}{U_{\max}^2}, \qquad (16)$$

which is roughly (ρ_2/ρ_1) times bigger. The two bounds above provide us with an estimate of the size of the computational domain for use in simulations.

The growth rates of the unstable modes have been evaluated for a variety of density ratios and wind profiles in Ref. 18. In Fig. 2 we show the growth rates for a wind profile given by Eq. (1) for $r=0.1$ and for five different values of G relevant to those examined numerically.

For large values of G, it has been shown by Ref. 18 and proven in Ref. 19 that the growth rate has an exponential dependence on the parameter G (e.g., $k\mathrm{Im}\{c\} \sim e^{-4.9\ A_t G}$). This dependence puts a strong restriction on the range of G
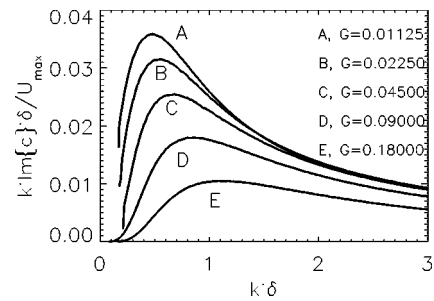

FIG. 2. The linear growth rate as a function of the wave number. Each curve corresponds to a different value of $G \equiv g\delta/U_{\max}^2$ used in our simulations.

that can be examined in numerical simulations. For large values of G the time scale for a wave to grow is much smaller than the period of the wave and therefore requires many wave crossing times before the nonlinear regime is obtained. Finally we note that the growth rate has shown a weak dependence on compressibility.

B. Weakly nonlinear theory

Weakly nonlinear theory examines the asymptotic cases when a system is marginally stable and is based on an expansion in terms of a small parameter. For the KH case, such an analysis has been performed by Ref. 4. For the wind profile as in Eq. (1), the study of the generation of gravity waves in the weakly nonlinear regime was further examined in Refs. 28 and 19. This analysis holds for for weak winds ($G \gg 1$) and/or for small density ratio $r \ll 1$. It demonstrates that nonlinearities first become important inside the critical layer. The resulting flow is a vortex traveling with the gravity wave. The initial exponential growth transitions to an oscillating power law growth ($t^{2/3}$) proportional to the viscosity. This transition happens at amplitudes $h/\lambda \sim (k\mathrm{Im}\{c\}\delta/U_{\max})^2$. Using Lagrangian tracers, it was shown that mixing is most important at the separatrix of the flow (the location where two corotating vortices meet). A similar behavior appears in our simulations for the modes for which the cusp of the wave breaks.

C. Free waves and theory of the highest wave

Finally we review those properties of free (no wind) irrotational finite amplitude waves that will be useful in this work. It has been known for some time[29] that the Stokes equations for irrotational flows have solutions of traveling gravity waves. These have been evaluated and tabulated in Ref. 30. There is a highest amplitude, given by $Ak=0.4432$, for which gravity wave solutions exist. At this amplitude the waves form a singular crest such that the radius of curvature of the interface at the crest goes to zero, forming a corner with opening angle of 120°. The stability properties of these waves have been studied extensively by Longuet-Higgins[31] and references therein. It has been shown that the crest itself is subject to various instabilities. Subharmonic instabilities appear in front of the crest of the wave when the amplitude of the wave is larger than $Ak=0.4292$. However, when superharmonic instabilities are allowed (more than one wavelength in the computational domain is considered) the crests

of the waves become unstable at much smaller amplitudes.[32] The nonlinear development of the instabilities has been shown to lead to breaking of the crest.[33] In our simulations the gravity waves are close to irrotational since the initial perturbation has no vorticity and vorticity is conserved up to viscous time scales (in the absence of boundary layers). There are similarities, therefore, between our simulations and the free wave theory. In particular, most of the instabilities described by Ref. 31 are present in our simulations as secondary instabilities in the fully developed waves, which affect the mixing properties of the flow. The presence of wind, however, results in differences of the nonlinear development of these secondary instabilities even for slowly growing waves (weak winds), especially at structures in the breaking crest.

IV. NUMERICAL METHOD

All the numerical simulations described in this paper were performed using the FLASH code, a parallel, adaptive-mesh simulation code for studying multidimensional compressible reactive flows found in many astrophysical environments. It uses a customized version of the PARAMESH library[34,35] to manage a block-structured adaptive grid, adding resolution elements in areas of complex flow. The models used for simulations assume that the flow is described by the Euler equations for compressible, inviscid flow. FLASH regularizes and solves these equations by an explicit, directionally split method, carrying a separate advection equation for the partial density of each chemical or nuclear species (scalars) as required for reactive flows. The code does not explicitly track interfaces between fluids. As a result, mixing occurs on grid-spacing scales exclusively due to numerical diffusion; the rate of this diffusion is a decreasing function of resolution, but is also a function of flow speeds and structure. Complete details concerning the algorithms used in the code, the structure of the code, selected verification tests, and performance may be found in Refs. 24–26.

V. NUMERICAL SIMULATIONS

Figure 3 illustrates the parameter space spanned by our simulations. Each block in this diagram corresponds to a set of simulations differing only in resolution and initial perturbation. The horizontal axis indicates the size of the computational domain in terms of the nondimensional number L, which varies by factors of 2 across the figure. The vertical axis corresponds to the parameter G, which also increases by powers of 2 going down the diagram, ranging from 0.011 25 to 0.18. The dashed line shows the location of the most unstable wave number as predicted by the linear theory. The two vertical thick lines show the location of the two maximum wavelengths given by the KH theory [λ_{KH} from Eq. (16)] and via Miles theory [λ_R from Eq. (15)]. Modes with wavelength to the right of each line are stable to the corresponding instability. For each location in the diagram more than one simulation has been performed with a different grid size. The index N corresponds to the number of grid points in each direction, ranging from 64 to 2048. Furthermore, we test for sensitivity of our results to the initial conditions by

L \ G	0.112	0.225	0.450	0.900	1.800	3.600	7.200
0.0112	$A1_N^{S/M}$	$A2_N^{M}$	$A3_N^{M}$	$A4_N^{M}$	$A5_N^{M}$		
0.0225		$B2_N^{S/M}$	$B3_N^{M}$	$B4_N^{M}$	$B5_N^{M}$	$B6_N^{M}$	$B7_N^{M}$
0.0450			$C3_N^{S/M}$	$C4_N^{M}$	$C5_N^{M}$		
0.0900				$D4_N^{S/M}$	$D5_N^{M}$	$D6_N^{M}$	$D7_N^{M}$
0.1800					$E5_N^{S/M}$		

FIG. 3. The parameter space spanned by our runs. Each block in this diagram corresponds to a set of different runs with different resolution N. The x axis gives the size of the computational domain measured in units of U_{max}^2/g; the y axis gives the value of $G \equiv g\delta/U_{max}^2$. The dashed line indicates the wavelength of the most unstable mode for a given value of G. The index S/M indicates whether a single-mode or multimode perturbation was imposed.

carrying out runs with varying spectrum of the initial wave perturbation. The superscripts M/S indicate whether a single mode (S) or a random multimode (M) perturbation was used at $t=0$. The strategy followed in our numerical simulations was to start from a computational domain the size of the most unstable wavelength for a given value of G and move to the right in the diagram (increasing L). The details of each run will be presented along with our results.

At this point we should comment on the computational limitations of the system we are investigating. First of all we cannot perform runs for very large L (too far to the right in our diagram) because in order to resolve the most unstable wavelength, we must increase the size of our grid beyond what is computationally feasible. For similar reasons, we cannot investigate very large values of the parameter G (too far down in the diagram) because the growth rate of the unstable modes becomes very small compared to the wave period and the diffusive time scale. The wavelength of the most unstable mode becomes larger and, as is shown later, more resolution is required to capture the physics of the wave breaking.

VI. WAVE DYNAMICS

A. Comparison with theory

In the first part of our investigation we focus on the formation and nonlinear development of the gravity waves. In order to verify the simulation results, we compare the growth rates of the gravity waves from the simulations with the rates predicted by the linear theory. In Fig. 4 we show the potential energy of the gravity waves at the early stages as a function of time for different values of the parameter G. The results are from the runs $A1_{512}^{S}$, $B2_{512}^{S}$, $C3_{512}^{S}$, $D4_{512}^{S}$, and $E5_{512}^{S}$ for a single-mode perturbation. Density plots of these runs can be seen in Fig. 6, which will be discussed later. The potential energy of the gravity wave was evaluated based on the integral
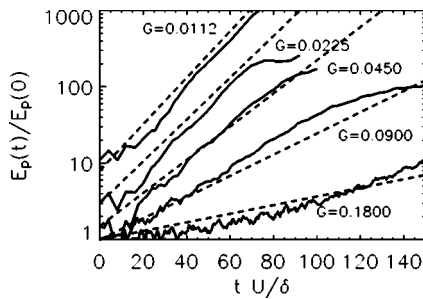
FIG. 4. Comparison of the observed growth rate with the linear theory. The solid black lines show the evolution with time of the potential energy $E_p(t)$ of gravity waves calculated from the numerical simulations $A1_{512}^S$, $B2_{512}^S$, $C3_{512}^S$, $D4_{512}^S$, and $E5_{512}^S$. The dashed lines give the linear theory predictions. The first three lines have been shifted up for clarity.
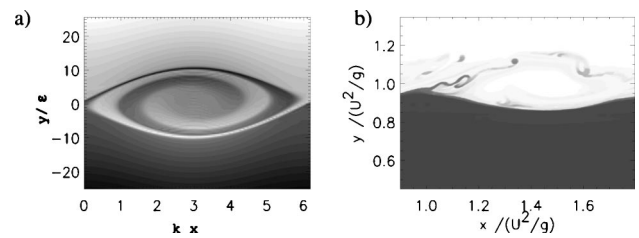

FIG. 5. A qualitative comparison of structure between weakly nonlinear theory and the numerical simulations. Panel (a) shows a contour plot of the vorticity as predicted by weakly nonlinear theory. Panel (a) shows a contour plot of density from our numerical simulations.

$$E_p = \frac{1}{2}(\rho_2 - \rho_1)g \int h(x)^2 dx, \qquad (17)$$

where $h(x)$ is the location of the interface, defined as the contour line where $\rho(y) = 0.98\rho_2$. Equation (17) was derived by integrating ρy over space and assuming that the wave amplitude is much smaller than the pressure scale height. We note that this method was the least noisy method to calculate the gravity wave potential energy in the linear regime. A direct integration over the whole computational domain for the evaluation of the potential energy was far too noisy. The results from the simulations for the evolution of the potential energy of the gravity waves as a function of the rescaled time tU/δ (from now on we drop the index "max" from U_{max} for convenience) are shown in Fig. 4 where they are compared with linear theory predictions. They are found to be in satisfactory agreement with the theory.

It would be useful to further verify our code using the results of weakly nonlinear theory. However, computational limitations did not allow us to reach close to the asymptotic regime $G \gg 1$ required to justify the comparison. Nonetheless, a qualitative comparison can be made. The two panels in Fig. 5 show a comparison of two advected fields: the vorticity as predicted by weakly nonlinear theory in panel (a), and the density from our numerical simulations in panel (b). There is obvious similarity in the structures of the two fields, although more small scale structure appears in panel (b).

B. Nonlinear evolution

Next we discuss results from the simulations when the system is far away from linearity. We present first the single-mode runs $A1_{512}^S$, $B2_{512}^S$, $C3_{512}^S$, $D4_{512}^S$, and $E5_{512}^S$. In each simulation a single mode was excited with wavelength equal to the box length. With this choice we are examining the evolution of the mode close to the most unstable one for each value of G. The panels in Fig. 6 are density plots that show the time evolution of the forming wave. Each row corresponds to a different value of G and each column represents a different time.

There is a difference in the structures that appear as we increase the parameter G. At smaller values of G we observe that as the wave grows, at some point in time a breaking cusp

forms from which material begins to mix. As time progresses, the wave becomes very oblique, with amplitude larger than that predicted by the theory of the highest wave.[31] The wave then overturns, leading to the generation of small scale structure and strong mixing.

As we increase the value of G, waves grow more slowly as predicted by linear theory. In run $D4_{512}^S$ the wave reaches a maximum amplitude and forms a cusp. We note that this amplitude is smaller than that predicted by Michell[29] who assumed in his analysis that there was no upper fluid. The profile of the interface strongly resembles those calculated for irrotational waves by Ref. 30 for amplitudes close to the maximal one. The opening angle is roughly estimated to be 136°, which is close to, but a little wider than, the one predicted by Ref. 29. Figure 7 shows a density plot of a wave about to break and illustrates the opening angle. We note that due to the presence of the wind there is an asymmetry with respect to front and the back of the wave (i.e., the wave is tilted forward). The development of cusp instabilities and the further input of energy from the wind leads to the ejection of material from the cusp at aperiodic time intervals. The ejected material diffuses in an eddy turnover time in the upper fluid. At each ejection, the amplitude of the wave drops. The wave resumes growing, forming a new cusp that again leads to the ejection of new material and so on. Finally, in the last row of Fig. 6, $G = 0.18$, it appears that almost no cusp formation or mixing is present. As we will show later in the resolution studies, this is an effect of low resolution that suppresses the cusp instabilities described earlier. In finite-difference-based or finite-volume-based simulations, the appearance of instabilities—such as cusp formation—can critically depend on the (effective) grid resolution. This fact is a strong motivation underlying the resolution studies presented later on.

There is an interesting interpretation of the above described results related to the two instabilities (KH and resonant) described in the linear theory. For the runs $A1_{512}^S$, $B2_{512}^S$, and $C3_{512}^S$ (where the overturning mechanism appears to be more dominant), the wavelength of the most unstable wave is smaller than the maximum wavelength λ_{KH} predicted by KH theory. On the other hand, for the runs $D4_{512}^S$, $E5_{512}^S$ where there is only cusp breaking or no mixing at all, the most unstable wavelength is larger than λ_{KH}. The minimum wave number predicted from KH can therefore be interpreted as a criterion for overturning to occur.

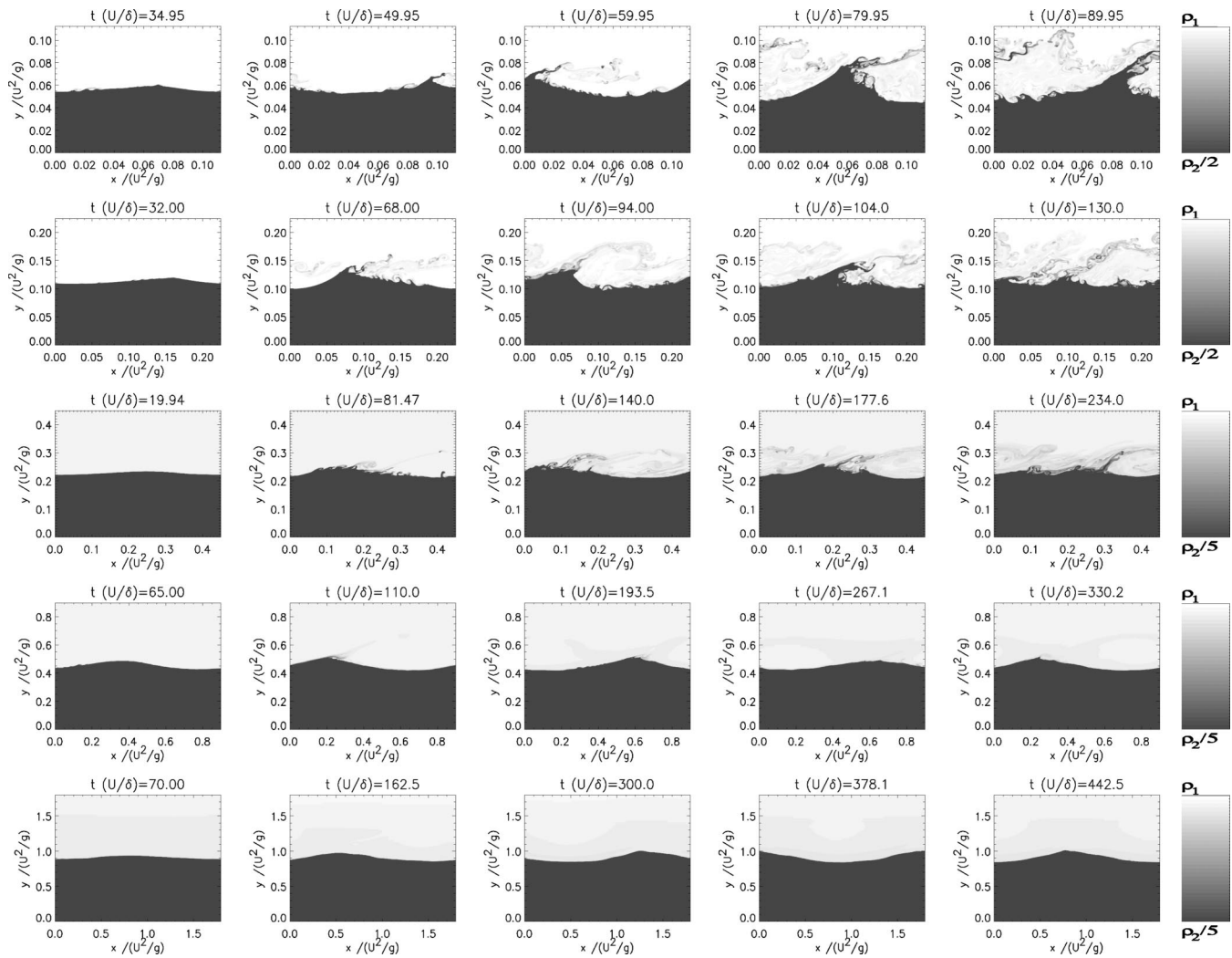Important differences appear when we move to multi-

FIG. 6. Waves forming for single-mode initial perturbations for different values of G. The gray scale represents density. Each row corresponds to a different value of G (starting from the smallest value in the top row) $G=0.0112,0.0225,0.0450,0.0900,0.1800$; time increases from left to right. The computational domain is arranged so that the largest wavelength is close to the most unstable mode.

mode perturbations and computational boxes larger than the most unstable wavelength. There are two main reasons for this. The first is that larger boxes allow for vortex merging, which affects the dynamics of the waves. The second reason is that superharmonic instabilities lead to cusp breaking at smaller amplitudes than for cases in which only a single wave period is considered.[32] Figure 8 shows contour plots of the mass fraction of the lower fluid X from the evolution of the runs $A5_{512}^{M}$, $B5_{512}^{M}$, $C5_{512}^{M}$, $D5_{512}^{M}$, and $E5_{512}^{M}$. All runs have the same multimode perturbation as described in Sec. II, the same box size L, and resolution N. In the first three rows mixing is initiated by the overturning of small, most unstable, waves, and a thin mixed layer is formed. Vortices merge, exciting larger wavelengths that themselves overturn leading to a wider mixed layer. This procedure continues until wavelengths larger than λ_{KH} are excited. Mixing then continues at a smaller rate in a mechanism that resembles cusp breaking, although an interface cannot be defined in this case.

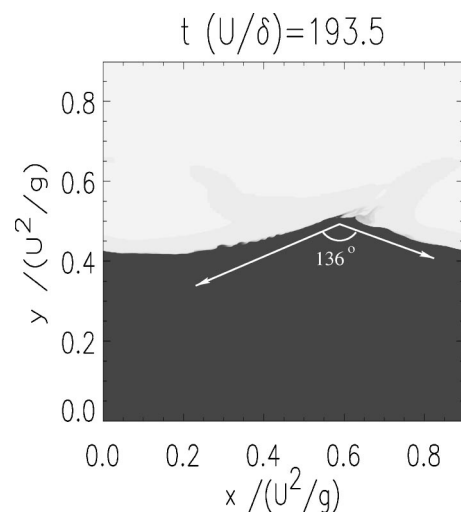For larger G, modes with large wavelengths appear to be

FIG. 7. The structure of the wave near cusp breaking. The wave, just before breaking, forms a cusp of angle $\sim 136°$. The amplitude of the wave at this point is $Ak=0.35$. The presence of the wind makes the breaking possible at smaller values of the amplitude than the theory of free waves predicts.
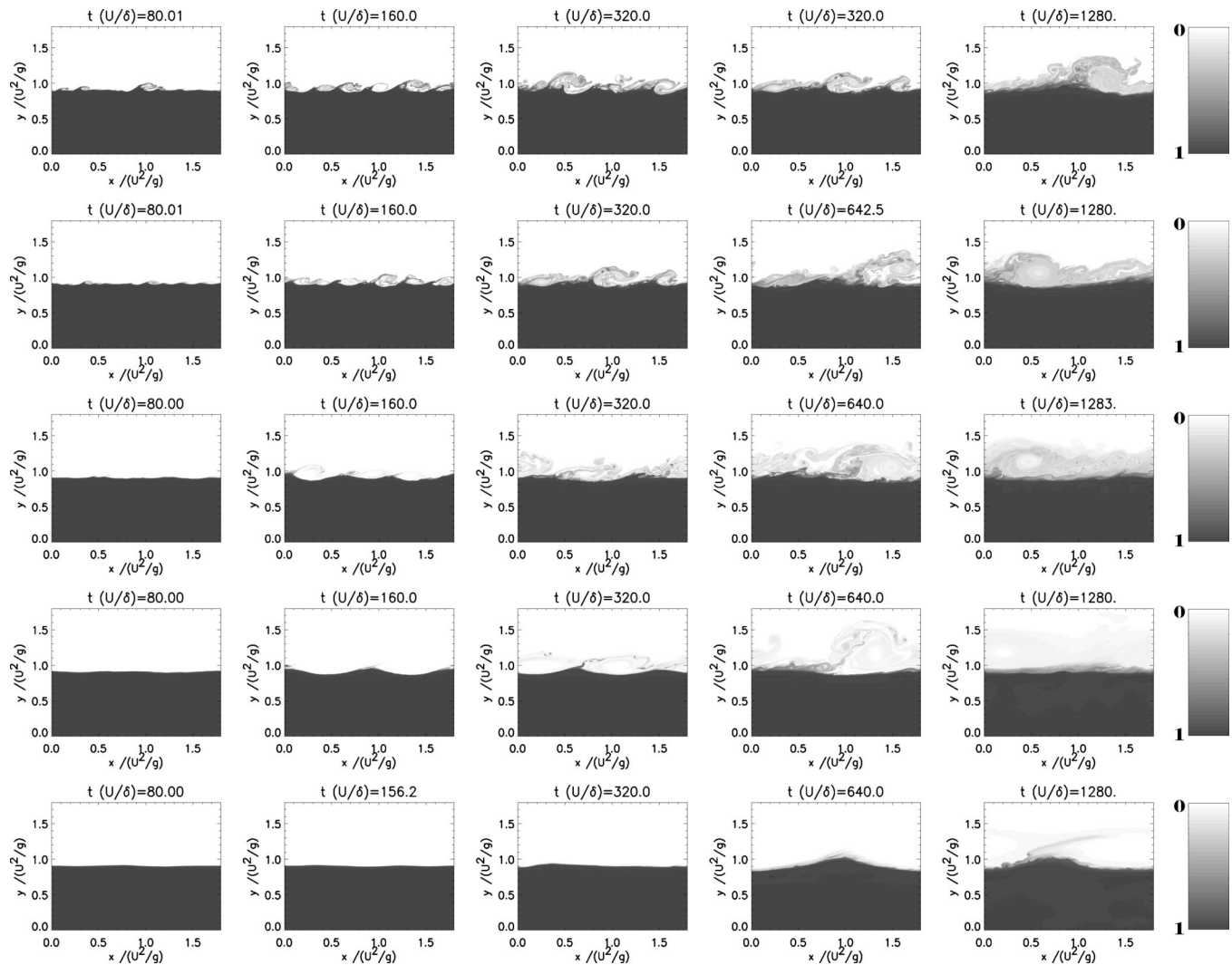
FIG. 8. Waves forming for different G and the same L with random multimode perturbations. The gray scale represents the mass fraction X. Each row corresponds to a different value of G (starting from the smallest value in the top row) $G=0.0112, 0.0225, 0.0450, 0.0900, 0.1800$; time increases from left to right. The computational domain for all figures shown here is $L=1.8$.

dominant from the beginning. In particular, the mode with $l_x/\lambda = k\delta L/2\pi = 2$ (two wave peaks in the box) is dominant at the beginning of the $D5_{512}^M$ run, and the mode with $l_x/\lambda = 1$ is dominant for the run $E5_{512}^M$. We note that for incompressible flows, the linear theory predicts that the most unstable wavelength has $l_x/\lambda \simeq 2.5$ for the $D5_{512}^M$ run and $l_x/\lambda \simeq 1.7$ for the $E5_{512}^M$ run, which is close to our result considering that the ratio l_x/λ in our setup can take only integer values. Furthermore, mixing seems to be suppressed for the $E5_{512}^M$ run until late times, while the run $D5_{512}^M$ forms breaking cusps that eject material in the upper fluid that can be clearly seen in the third panel of the fourth row in Fig. 8. We note that there is more mixing than the single-mode run with the same value of G because, as we discussed in Sec. III C, the presence of superharmonic instabilities forces the cusps to break at smaller wave amplitudes. At the end of this run, the two waves have merged into one.

We focus further on the run $D5_{512}^M$, which has interesting properties regarding the evolution of superharmonic perturbations. The configuration of two traveling waves shown in the first three panels of the fourth row of Fig. 8 appears to be

stable to small perturbations (noise) since it remains at this configuration for some time. Superharmonic instabilities, although leading to more cusp breaking, do not destroy the two vortex configuration initially. However, eventually the two vortices do merge, exciting the mode with wavelength equal to the box size and causing significant mixing. We further investigate the run $D5_{512}^M$ by considering cases with different perturbations imposed at $t=0$; the same functional form for the spectrum of perturbations was used [Eq. (11)], but with the peak of the spectrum at values $k_{max} = 3k_0, 4k_0, 5k_0$ compared to $2k_0$ as in the original run. The first case corresponds to the previously described run. Although the same mode $(k=2k_0)$ appears to be dominant at the beginning, the time at which the two vortices merged into one was different for each run and varied from $200\delta/U$ to $500\delta/U$. We note that there was no systematic correlation of the merging time with k_{max}. Figure 9 shows the evolution of the potential energy for these runs, with diamonds indicating where the two vortices merged.

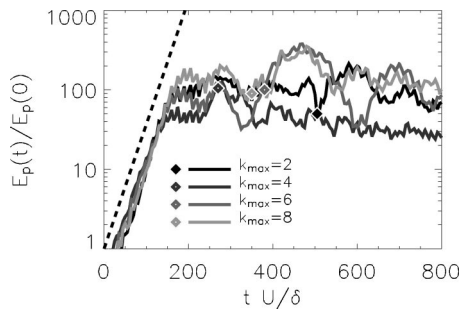It would be interesting to investigate the energy transfer across the exited modes and measure the resulting spectrum

FIG. 9. The evolution of the gravity wave potential energy for different initial perturbations for the runs $D5_{512}^M$. The diamond indicates when the two waves merged into one. The dashed line gives the linear theory prediction.

and compare with theoretical predictions.[36] However, the computational domain in our runs is not big enough to include a large number of modes. Furthermore, it is worth noting that at the end the largest wavelength mode is dominant, implying that the two-dimensional cascade has influenced our results. Although one can trust the two-dimensional assumption when mixing starts, three-dimensional effects may well become important when vortex merging happens. Thus vortex merging can be the result of the two-dimensional inverse cascade, and might not take place in a three-dimensional (3D) setup, resulting in a different structure of the mixing zone for the 3D case. The behavior, therefore, of the 2D runs must be compared with 3D runs in order to resolve this issue.

VII. MIXING

Next we focus on mixing. The primary quantities of interest to us are the amount of mass of the lower fluid that is mixed upwards and the distribution of this mixed mass. As discussed in Sec. IV, in these simulations mixing on small scales is due to uncontrolled numerical diffusion. Despite this, our investigation is based on the assumption that absent this effect, mass will still be mixed at a finite rate indepen-

dent of the diffusivity because of the generation of eddies at smaller and smaller scales (turbulent diffusion). How close we are to this limit will be demonstrated in the following section, where we present our convergence studies. Furthermore, since our results are from run-down numerical experiments, at late times, where large-scale turbulence has decayed, only numerical diffusion will give effective mixing. Therefore, there are two expected stages of mixing: dynamic mixing at early times that is dominated by small scale generation (cusp breaking and overturning) and a diffusive stage at late times when turbulence is no longer present.

Keeping the above in mind, we quantify the mixing by measuring the lower fluid mass inside a mixed layer and averaging over the horizontal direction. The mixed layer is defined as the region in our computational domain where the concentration of the passive scalar X [defined in Eq. (9)] is between two extreme values X_{max} and X_{min}. We define, therefore, the quantity $M(t, X_{min}, X_{max})$ as the mixed mass per unit area located in the layer with $X_{min} < X(t, x, y) < X_{max}$,

$$M(t, X_{min}, X_{max}) = \frac{1}{l_x} \int_{\mathcal{D}} \rho X \, dx \, dy, \tag{18}$$

where $\mathcal{D} = \{(x, y) | X_{min} < X(t, x, y) < X_{max}\}$. We further define the density distribution of the mass as

$$\mu(t, X) \equiv dM(t, X_{min}, X)/dX. \tag{19}$$

The distribution expresses the amount of mass from the lower fluid that lies between the values X and $X + dX$, per unit area, and is of particular interest when the effect of chemical or nuclear reactions is studied.

In Fig. 10 we plot $\mu(t, X)$ for the runs $A5_{1024}^M$, $B5_{1024}^M$, $C5_{1024}^M$, $D5_{1024}^M$, and $E5_{1024}^M$. The distribution was calculated by averaging over space and time for the time range $1200 < tU/\delta < 1500$. The first three runs $A5_{1024}^M$, $B5_{1024}^M$, and $C5_{1024}^M$ (overturning runs) have significant mixed mass in the range $0.02 < X < 0.4$, with a small shift of the peak of the distribution toward smaller values of X as G is increased.
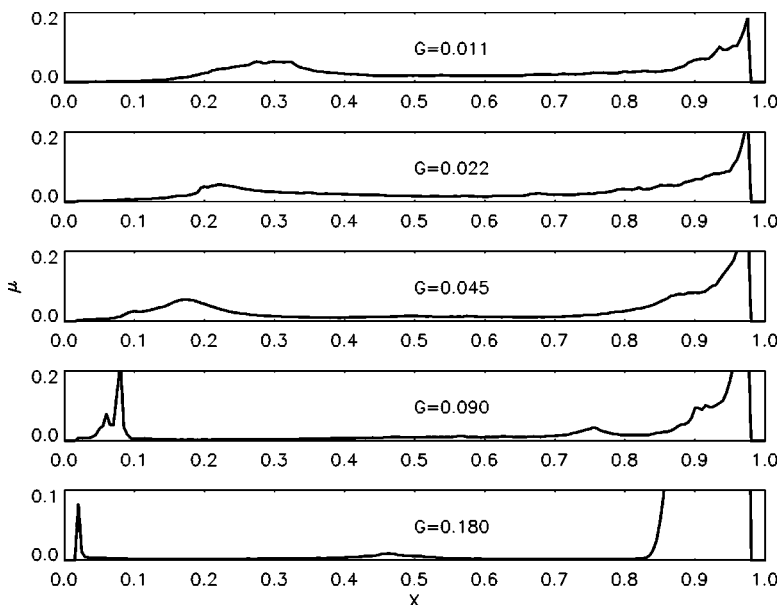

FIG. 10. Distribution of mass μ in the mixed layer for the 1024^2 runs with $L = 1.80$ and different values of G; the value of G is increasing as we move from top to bottom.
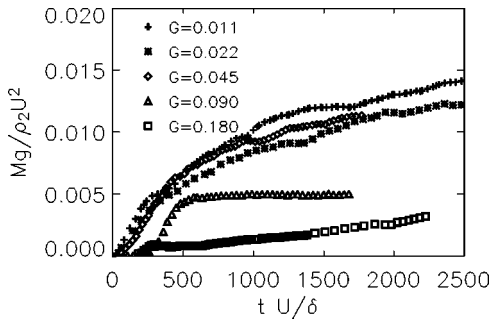
FIG. 11. The evolution of the mass in the mixed layer per unit area $M(t,0.02,0.4)$ with $L=1.80$ and different values of G, as indicated.
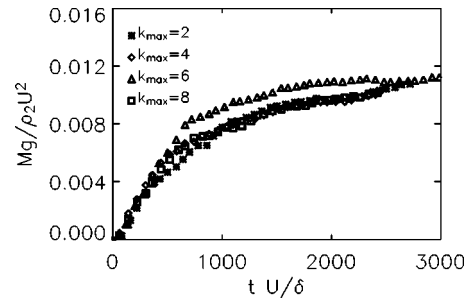

FIG. 12. The amount of mass in the mixed layer $M(t,0.02,0.4)$ for different initial perturbations for the run $B5^M_{512}$ ($G=0.0225$).

There is a striking difference between these runs and the results from $D5^M_{1024}$, $E5^M_{1024}$ (cusp-breaking runs). The peak of the distribution of the cusp-breaking runs are at smaller values ($X<0.2$) with much smaller deviation (much narrower distribution peaks). This implies that for the cusp-breaking mechanism, mixed mass spreads over a larger area than in the overturning mechanism. Mixing by overturning is confined in the region of the wave, while the ejected material from the cusp breaking can spread over a wider vertical range.

In all runs a significant amount of mass appears to be in the high X end of the distribution. This result is more pronounced for the large G cases (e.g., $E5$). This mass is not related to the cusp formation or overturning but rather to numerical diffusion in the bulk of the wave. This phenomenon is more obvious in the large G runs only because the dynamical time scale (δ/U) is large and closer to the numerical diffusion time scale. This mixed mass strongly depends on the resolution, an effect that is not desirable. We are therefore only interested in the mixed mass for low X and we will therefore restrict our attention in estimating the mixed mass in the range $0.02 \leqslant X \leqslant 0.4$.

Figure 11 shows $M(t,0.02,0.4)$ as a function of the rescaled time (tU/δ) from the runs $A5^M_{1024}$, $B5^M_{1024}$, $C5^M_{1024}$, $D5^M_{1024}$, and $E5^M_{1024}$. The first three curves ($G \leqslant 0.045$) in which mixing is due to overturning give similar results with small differences. The mixing time scale for those runs is determined by (δ/U). This implies that the mixed mass as a function of time for the given box size and small values of the parameter $G(G \leqslant 0.045)$ is given by

$$M(t,0.02,0.4) = \rho_2 \frac{U^2}{g} f(tU/\delta), \tag{20}$$

where f is a function that can be estimated from Fig. 11. The total amount of mass mixed in the dynamic mixing range for sufficiently small δ is therefore, to first order, independent of the wind length scale δ, and only the time scale depends on δ. The amount of mixed mass increases linearly at early times (dynamical range), with a rate given by

$$\frac{dM}{dt} = \alpha_1 \frac{\rho_2 U^3}{g\delta}, \tag{21}$$

where α_1 is measured to be $\alpha_1 \simeq 1.5 \times 10^{-5}$.

The dynamical mixing appears to transition to a slower rate, which is possibly related to numerical mixing, after $t \simeq 2 \times 10^3 \delta/U$. The total amount of mass mixed at this point is

$$M = \alpha_2 \rho_2 U^2/g, \tag{22}$$

where α_2 is measured to be $\alpha_2 \simeq 1 \times 10^{-2}$.

As we move to higher values of the parameter G (runs $D5^M_{1024}$ and $E5^M_{1024}$), the above results no longer hold. The amount of mass mixed for the runs $D5^M_{1024}$ and $E5^M_{1024}$ deviates from the previously discussed curve: $M(t,0.02,0.4)$ appears to decrease fast with G when G is larger than 0.045. This behavior is expected because we know from the linear theory that the growth rate decreases exponentially with G. Also, from weakly nonlinear theory we know that the wave to first order remains linear (e.g., no cusp) in the limit of large G.

In order to draw conclusions about the behavior of chaotic nonlinear systems from numerical simulations, an ensemble average of different initial conditions is ideally required. However, the computational cost of high resolution runs does not allow for a large number of runs. For this reason, we have had to content ourselves with four different simulations of the setups in $B5^M_{512}$ and $D5^M_{512}$ with different imposed perturbations, and we have obtained only qualitative results about the sensitivity of the runs to small differences in the initial conditions. The results are shown in Figs. 12 and 13. For the $B5^M_{512}$ runs fluctuations of M are small throughout the integrated time, while for the runs $D5^M_{512}$ there are significant variations of the amount mixed. The chaotic behavior of the two vortex configuration, as discussed in the preceding section, explains the existence of the large fluctua-
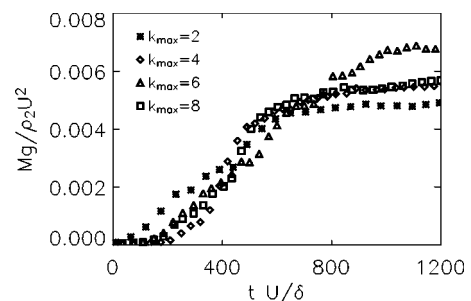

FIG. 13. The amount of mass in the mixed layer $M(t,0.02,0.4)$ for different initial perturbations for the run $D5^M_{512}$ ($G=0.09$).
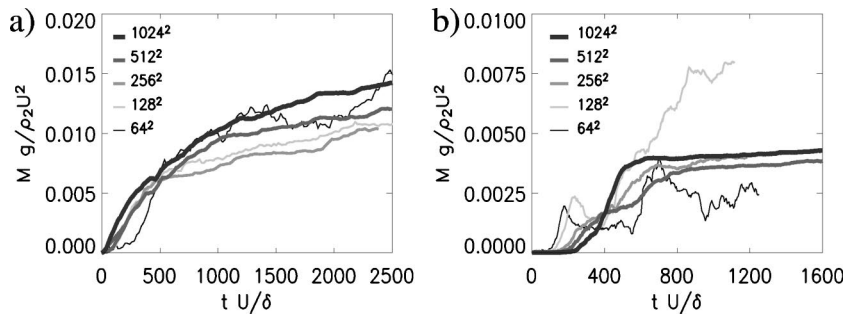
FIG. 14. The evolution of the mixed mass $M(t,0.02,0.4)$ for the runs $B5_N^M$, $G=0.225$ [panel (a)] and $D5_N^M$, $G=0.09$ [panel (b)], for five different resolutions.

tions. The sensitivity, therefore, of M to the initial imposed perturbation increases as we increase the parameter G, and one therefore should be careful when interpreting the results of a single run.

VIII. CONVERGENCE STUDIES

One of the key issues of the problem we examine is the mixing of the two species and it is, therefore, important to control diffusion. Unfortunately we have to rely on numerical diffusion, which is not a well-controlled quantity, for mixing on small scales. It is believed that in the limit of high resolution (high effective Reynolds number), the effective diffusion of the two species will reach an asymptotic value independent of the resolution. This expectation is based on the belief that once fully developed turbulence appears, effective diffusion would be determined by eddy diffusion. This assumption, and how close to this limit our simulations are, needs to be explicitly tested.

To investigate the dependence of $M(t,X_{\min},X_{\max})$ with resolution we repeated the same runs with different N and looked at the dependence of M and μ on the grid size. In Fig. 14 we show the mixed mass $M(t,0.02,0.4)$ as a function of time for the runs $B5_N^M$ and $D5_N^M$ for different values of N ranging from 64 to 1028. A similar effect is observed for all the overturning runs. As we increase the resolution of each run, the amount of mass mixed M decreases initially up to some point of lowest mixing and then starts increasing again [see Fig. 14(a)]. This is consistent with the idea that at low resolution, numerical diffusion dominates the mixing so that increasing the resolution decreases total mixing. Eventually, however, the mixing becomes dominated by mixing due to small scale motions, and increasing the resolution further increases the total mixing as smaller and smaller eddies are resolved. A more complex behavior was observed for the cusp-breaking waves as we increased resolution [see Fig.

14(b)]. The results for the cusp breaking runs suggest that at higher resolution, the amount of mass mixed becomes only weakly dependent on resolution. Nonmonotonic dependence on resolution of large scale flows has been observed in simulations of Rayleigh–Taylor instability even when atomic mixing rates have converged.[26,37] Although the mechanisms that are involved in numerical dissipation and the effect of resolution on numerical simulations are qualitatively understood, a quantifying theory for its effect is not available. To further demonstrate the sensitivity of mixing with resolution for the large G runs, we show in Fig. 15 the results of the simulations $E5_N^M$ for different resolutions: the structure of the cusp changes drastically as we increase the resolution.

Another limit of interest is $L \to \infty$. It is expected that if we chose sufficiently large L, then horizontally averaged quantities should not depend on L. To test how close we are to this limit, we performed a number of simulations changing the value of L while keeping the resolution per unit of physical length, N/l, fixed. It was found that larger values of L were required for convergence as we increased G. In Fig. 16 we present the dependence of $M(t,0.02,0.4)$ on the size of the computational domain L for two values of G ($G=0.0112$ and $G=0.09$). Although the runs with small G converged for L as small as 0.9, for the large G modes convergence seems to be achieved only when L is larger than 7.2.

IX. CONCLUSIONS

In this paper we presented the results from an extensive investigation of wind-driven gravity waves using numerical simulations. Motivated by an astrophysical problem, we investigated how interfacial waves are amplified by the wind, following the resonant mechanism of Miles[8] to the nonlinear (breaking wave) stage. Keeping the density ratio fixed at $r=0.1$, we performed a parameter study by changing the nondimensional parameter $G=g\delta/U^2$.
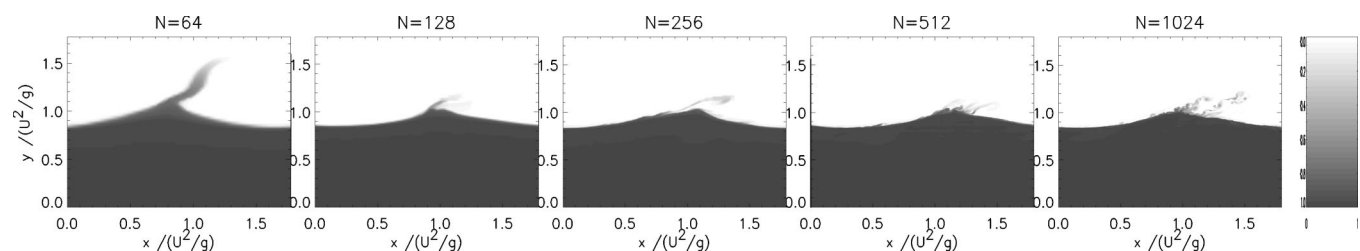

FIG. 15. The formation of the cusp with different resolutions. N gives the number of grid points across the computational domain. The figures are taken from the runs $E5_N^M$ for the value of $G=0.18$.
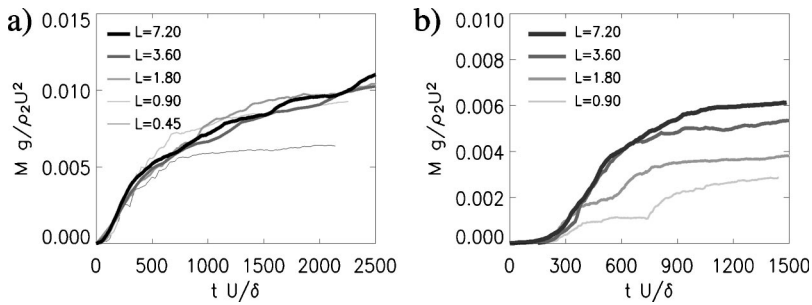
FIG. 16. The evolution of the mixed mass $M(t, 0.02, 0.4)$ for the runs $B5_N^M$, $G=0.225$ [panel (a)] and $D5_N^M$, $G=0.09$ [panel (b)] and for five different box sizes L. The resolution per unit length (N/L) was kept fixed in all runs to $256/0.9$.

At early times, our results are in quantitative agreement with the linear theory and qualitative agreement with weakly nonlinear theory. In the nonlinear stage our results indicate that the initial exponential growth of gravity waves predicted by Miles's theory reaches saturation. For small values of G, this saturation occurs via overturning of the gravity waves. For larger values of G, the waves saturate without overturning. At the saturation amplitude secondary instabilities appear near the cusp of the wave, resulting in cusp breaking. These instabilities closely resemble the instabilities of irrotational finite amplitude gravity waves seen previously.[31] Our results therefore demonstrate a connection between Miles[8] theory for the generation of waves by wind and the theory for finite amplitude irrotational waves.

The transition between the formation of overturning waves (smaller values of G) and the formation of cusp-breaking waves (larger values of G) occurs close to the value of G at which the most unstable wavelength is also marginally KH unstable. We denote this critical value of G as G_T, and estimating from the linear theory, we find $G_T \simeq 0.07$. The waves for the runs with $G < G_T$ (i.e., A, B, C) were found to overturn, while the waves for the runs with $G > G_T$ (i.e., D, E) showed cusp breaking. Therefore, the transition from overturning to cusp breaking waves can be estimated from linear theory. Of course, the validity of such a result for different density ratios still needs to be examined.

The mixing properties of the two regimes (small G and large G) are significantly different. The overturning regime mixes an amount of mass per unit area that scales as $\rho_2 U^2/g$ on a time scale δ/U. On the other hand, for large G mixing occurs via secondary instabilities, a smaller amount of mass is mixed, and the distribution of the mixed mass is different.

Mixing was found to depend on the resolution for all cases, but more strongly in the cusp-breaking runs. It was found that at high enough resolutions, the amount of mass mixed increases with resolution. Our mixing results, therefore, can be interpreted only as a lower bound on the amount of mass mixed. We found better convergence in the limit $L \rightarrow \infty$ but a higher L (computational domain) was required to achieve this as we increased the parameter G.

We believe that the results of this paper can guide future investigations on wind-wave interactions and mixing in stratified media by wave breaking. In particular, it would be interesting to know if cusp breaking occurs for arbitrarily large values of G or if there is a cutoff. Also, the effect of different density ratios, dimensionality, and surface tension would be of interest. Finally, we emphasize that there is al-

ways a need to verify such results by comparing solutions obtained by different numerical methods as well as to validate the calculations with experimental data.

[1] H. Helmholtz, "Ueber discontinuirliche Flüssigkeitsbewegungen," in *Wissenschaftliche Abhandlungen* (Johannes Ambrosius Barth, Leipzig, 1882), pp. 146–157.

[2] Lord Kelvin, "Influence of wind and capillarity on waves in water supposed frictionless," in *Mathematical and Physical Papers IV Hydrodynamics and General Dynamics* (Cambridge University Press, Cambridge, 1910), pp. 76–85.

[3] S. Chandrasekhar, *Hydrodynamic and Hydromagnetic Stability* (Dover, New York, 1981).

[4] P. Drazin, "Kelvin–Helmholtz instability of finite amplitude," J. Fluid Mech. **42**, 321 (1970).

[5] P. C. Patnaik, F. S. Sherman, and G. M. Corcos, "A numerical simulation of Kelvin–Helmholtz waves of finite amplitude," J. Fluid Mech. **73**, 215 (1976).

[6] W. Tauber and S. O. Unverdi, "The nonlinear behavior of a sheared immiscible fluid interface," Phys. Fluids **14**, 2871 (2002).

[7] W. H. Munk, "A critical wind speed for air sea boundary processes," J. Mar. Res. **6**, 203 (1947).

[8] J. Miles, "On the generation of surface waves by shear flows," J. Fluid Mech. **3**, 185 (1957).

[9] M. J. Lighthill, "Physical interpretation of the mathematical theory of wave generation by wind," J. Fluid Mech. **14**, 385 (1962).

[10] M. M. Shara, "Recent progress in understanding the eruptions of classical novae," Publ. Astron. Soc. Pac. **101**, 5 (1989).

[11] J. W. Truran, in *Essays in Nuclear Astrophysics*, edited by C. A. Barnes, D. D. Clayton, and D. N. Schramm (Cambridge University, Cambridge, 1982), p. 467.

[12] M. Livio, "Some aspects of the evolution of strongly interacting binary stars," Mem. Soc. Astron. Ital. **65**, 49 (1994).

[13] M. Livio, "Topics in the theory of cataclysmic variables and x-ray binaries," in *Interacting Binaries*, edited by H. Nussbaumer and A. Orr (Springer, New York, 1994), pp. 135–262.

[14] M. Livio and J. W. Truran, "Elemental mixing in classical nova system," Astron. Astrophys. **617**, 126L (1990).

[15] R. D. Gehrz, J. W. Truran, R. E. Williams, and S. Starrfield, "Nucleosynthesis in classical novae and its contribution to the interstellar medium," Publ. Astron. Soc. Pac. **110**, 3 (1998).

[16] R. Rosner, A. Alexakis, Y.-N. Young, J. W. Truran, and W. Hillebrandt, "On the C/O enrichment of novae ejecta," Astrophys. J. Lett. **562**, L177

(2001).

[17] A. Alexakis, A. C. Calder, A. Heger, E. F. Brown, L. J. Dursi, J. W. Truran, R. Rosner, D. Q. Lamb, F. X. Timmes, B. Fryxell, M. Zingale, and P. M. Ricker, "On heavy element enrichment in classical novae," Astrophys. J. **602**, 931 (2004).

[18] A. Alexakis, Y.-N. Young, and R. Rosner, "Shear instability of fluid interfaces: Stability analysis," Phys. Rev. E **65**, 026313 (2002).

[19] A. Alexakis, Y.-N. Young, and R. Rosner, "Weakly non-linear analysis of wind-driven gravity waves," J. Fluid Mech. **503**, 171 (2004).

[20] *Dynamics and Modeling of Ocean Waves*, edited by J. G. Komen, L. Cavaleri, M. Donelan, S. Hasselmann, and P. A. E. M. Janssen (Cambridge University Press, Cambridge, 1995).

[21] *Wind over Wave Couplings*, edited by S. G. Sajjadi, N. H. Thomas, and J. C. R. Hunt (Clarendon, Oxford, 1999).

[22] S. E. Belcher and J. C. R. Hunt, "Turbulent flow over hills and waves," Annu. Rev. Fluid Mech. **30**, 507 (1998).

[23] P. S. Sullivan and J. C. McWilliams, "Turbulent flow over water waves in the presence of stratification," Phys. Fluids **14**, 1182 (2002).

[24] B. Fryxell, K. Olson, P. Ricker, F. X. Timmes, M. Zingale, D. Q. Lamb, P. MacNeice, R. Rosner, J. W. Truran, and H. Tufo, "Flash: an adaptive mesh hydrodynamics code for modeling astrophysical thermonuclear flashes," Astrophys. J., Suppl. Ser. **131**, 273 (2000).

[25] A. C. Calder, B. C. Curtis, L. J. Dursi, B. Fryxell, G. Henry, P. MacNeice, K. Olson, P. Ricker, R. Rosner, F. X. Timmes, H. M. Tufo, J. W. Truran, and M. Zingale, "High performance reactive fluid flow simulations using adaptive mesh refinement on thousands of processes," in *Proceedings on Supercomputing*, 2000, http://sc2000.org/proceedings/

[26] A. C. Calder, B. Fryxell, T. Plewa, R. Rosner, L. J. Dursi, V. G. Weirs, T. Dupont, H. F. Robey, J. O. Kane, B. A. Remington, R. P. Drake, G. Dimonte, M. Zingale, F. X. Timmes, K. Olson, P. Ricker, P. MacNeice, and H. M. Tufo, "On validating an astrophysical simulation code," Astrophys. J. **143**, 201 (2002).

[27] M. Zingale, L. J. Dursi, J. Zuhone, A. C. Calder, B. Fryxell, T. Plewa, J. W. Truran, A. Caceres, K. Olson, P. M. Ricker, K. Riley, R. Rosner, A. Siegel, F. X. Timmes, and N. Vladimirova, "Mapping initial hydrostatic models in Godunov codes," Astrophys. J., Suppl. Ser. **143**, 539 (2002).

[28] V. P. Reutov, "The plasma-hydrodynamic analogy and the nonlinear stage of instability of wind waves," Izv., Acad. Sci., USSR, Atmos. Oceanic Phys. **16**, 938 (1980).

[29] J. H. Michell, "On the highest gravity waves on deep water," Philos. Mag. **36**, 430 (1893).

[30] J. M. Williams, "Limiting gravity waves in water of finite depth," Philos. Trans. R. Soc. London, Ser. A **302**, 139 (1981).

[31] M. S. Longuet-Higgins, "Progress toward understanding how waves break," *Proceedings of the 621st Symposium on Naval Hydrodynamics*, Cambridge, MA, 1997.

[32] M. S. Longuet-Higgins and E. D. Cokelet, "The deformation of steep surface waves on water: II Growth of normal modes instabilities," Philos. Trans. R. Soc. London, Ser. A **364**, 1 (1978).

[33] M. S. Longuet-Higgins and D. G. Dommermuth, "Crest instabilities of gravity waves. 3. Nonlinear development and breaking," J. Fluid Mech. **336**, 33 (1997).

[34] P. MacNeice, K. M. Olson, C. Mobarry, R. de Fainchtein, and C. Packer, NASA Technical Report CR-1999-209483, 1999.

[35] P. MacNeice, K. M. Olson, C. Mobarry, R. de Fainchtein, and C. Packer, "PARAMESH: A parallel adaptive mesh refinement community toolkit," Comput. Phys. Commun. **126**, 330 (2000).

[36] A. Pushkarev, D. Resio, and V. Zakharov, "Wind turbulent approach to the wind-generated gravity sea waves," Physica D **184**, 29 (2003).

[37] G. Dimonte, D. L. Youngs, A. Dimits, S. Weber, M. Marinak, S. Wunsch, C. Garasi, A. Robinson, M. J. Andrews, P. Ramaprabhu, A. C. Calder, B. Fryxell, J. Biello, L. Dursi, P. MacNeice, K. Olson, P. Ricker, R. Rosner, F. Timmes, H. Tufo, Y.-N. Young, and M. Zingale, "A comparative study of the turbulent Rayleigh–Taylor instability using high-resolution three-dimensional numerical simulations: The Alpha-Group collaboration," Phys. Fluids **16**, 1668 (2004).